MorphoCopter: Design, Modeling, and Control of a New Transformable Quad–Bi Copter

Harsh Modi ⬚, *Student Member, IEEE*, Hao Su*, Senior Member, IEEE*, Xiao Liang ⬚*, Member, IEEE*, and Minghui Zheng ⬚*, Member, IEEE*

Abstract—This article presents a novel morphing quadrotor, named MorphoCopter, covering its design, modeling, control, and experimental tests. It features a unique single rotary joint that enables rapid transformation into an ultranarrow profile. Although quadrotors have seen widespread adoption in applications, such as cinematography, agriculture, and disaster management, with increasingly sophisticated control systems, their hardware configurations have remained largely unchanged, limiting their capabilities in certain environments. Our design addresses this by enabling the hardware configuration to change on the fly when required. In standard flight mode, the MorphoCopter adopts an *X* configuration, functioning as a traditional quadcopter, but can quickly fold into a stacked bicopters arrangement or any configuration in between. Existing morphing designs often sacrifice controllability in compact configurations or rely on complex multijoint systems. Moreover, our design achieves a greater width reduction than any existing solution. We develop a new inertia and control-action aware adaptive control system that maintains robust performance across all rotary-joint configurations. The prototype can reduce its width from 447 to 138 mm (nearly 70% reduction) in just a few seconds. We validated the MorphoCopter through rigorous simulations and a comprehensive series of flight experiments, including robustness tests, trajectory tracking, and narrow-gap passing tests.

Index Terms—Adaptive, control, design, morphing, quadcopter.

Harsh Modi and Minghui Zheng are with the Department of Mechanical Engineering, Texas A&M University, College Station, TX 77843 USA (e-mail: harsh.modi@tamu.edu; mhzheng@tamu.edu).

Hao Su is with the Lab of Biomechatronics and Intelligent Robotics, Department of Biomedical Engineering, Tandon School of Engineering, New York University, New York, NY 11201 USA (e-mail: hao.su@nyu.edu).

Xiao Liang is with the Department of Civil & Environmental Engineering, Texas A&M University, College Station, TX 77843 USA (e-mail: xliang@tamu.edu).

I. INTRODUCTION

RECENT growth of commercially available drones has enabled widespread adoption in day-to-day life. Applications range from social cinematography to forest-fire detection [1], search and rescue [2], and medical delivery [3], among others. Among all the drone configurations, the quadcopter in an *X* arrangement is the most common due to its simplicity and robustness. However, it has a relatively large footprint relative to its payload dimensions, limiting its usability in applications that require these drones to pass through narrow gaps. One such scenario arises in the postdisaster search and rescue. The standard configuration drones must execute precisely planned tilt maneuvers to squeeze through narrow gaps [4], [5], [6]. During these maneuvers, the drone has to sacrifice lateral and vertical controllability, impeding mission safety and efficiency.

To achieve smooth flight through narrow gaps, we require a drone that can morph into a compact configuration temporarily while remaining controllable. It should also be able to revert to the standard configuration for efficient flight. One such example is the foldable drone that can squeeze and fly through narrow gaps [7]. However, this design requires four additional servomotors to control the four arms of the quadrotor independently, making it complex and prone to failures. Although it has the added benefit of controlling the arms independently for complex maneuvers, it does not reduce the width of the drone by a large amount. Similar designs, their dynamic modeling, and their control are available in [8], [9], [10], [11], [12], [13], [14], and [15]. Alternatively, the design in [16] demonstrates a quadrotor that can rotate the arms containing the front two propellers and aft two propellers independently to reduce the width using only two servomotors. However, this design is not controllable in a narrow configuration and merely becomes a projectile while passing through a narrow gap. The drone demonstrated in [17] has two bicopters stacked on top of each other, which can separate in flight and become two independent bicopters. However, this design can only have a standard X-quadcopter configuration or a two-independent bicopters configuration. Also, it cannot go back to the quadcopter configuration after the separation. The design in [18] uses a compliant mechanism-based quadrotor, which can crawl on the ground through a narrow gap but cannot fly through it. Similarly, the design in [19] uses a "crash to squash" approach to fold and uses terrestrial locomotion inside the narrow passage. This design also cannot "fly" through the narrow passage. Passively morphing quadrotors in [20] and [21] do not require any

This article has been accepted for inclusion in a future issue of this journal. Content is final as presented, with the exception of pagination.

2   IEEE/ASME TRANSACTIONS ON MECHATRONICS

actuators to morph, but they are not fully controllable during narrow configuration and require precise trajectory planning to provide sufficient momentum to pass through the narrow gap. The shrinking quadrotor demonstrated in [22] reduces the length of each arm symmetrically using the Sarrus-linkage mechanism with a maximum size reduction of only 24.4% . The flexible arms quadrotor shown in [23] can reduce the size by around 50% . However, in that design, the lift force reduces by around 80% in the narrowest configuration, limiting its maneuverability significantly. The design in [24] involves tilting the pairs of rotors such that the roll attitude of the quadrotor body can be controlled independently to very steep angles. However, this design requires two additional servomotors, and increases the size in the vertical direction significantly to pass through a narrow gap. The design in [25] requires interaction with the environment to fold. There are some other nonconventional designs of multirotor drones in [26], [27], [28], [29], [30], [31], and [32]. However, these designs involve complex mechanical and electronic components, which are too expensive and difficult to implement in day-to-day life. The designs in [33] and [34] are simple bicopter designs, which are controllable in x-y-z-yaw and can pass through narrow gaps. However, they cannot overcome the simplicity and controllability of the quadcopter configuration in normal flights.

To overcome the issues highlighted in the existing designs, we introduce a new morphing drone named MorphoCopter. Our design can be a standard X-quadcopter during a normal flight, which is the most efficient configuration and has almost equal maneuverability in both x and y directions. In addition, to pass through narrow gaps, it can fold in-plane about a central pivot joint, reducing its width continuously until it forms stacked bicopters. During all these configurations, the morphocopter is fully controllable in x-y-z-yaw. The specific prototype developed in this article has the width of 447 mm in a standard configuration, and 138 mm in a fully folded configuration. However, we only introduce the concept of this design through this article, and it can be scaled as per the requirement, making necessary changes in the hardware specifications and controller gains. The designs in [35] and [36] are similar to our design but have certain limitations. In [35], the quadrotor is normally in an X-configuration with the capability of folding at the center by $21°$ and $27°$. However, it cannot morph fully into a stacked bicopters configuration, limiting its width reduction capability. Also, it does not delve into controller adaptation due to changes in the configuration. The controller presented in [36] uses adaptive control to adjust with the changing dynamics, but their design can also reduce the size of the drone only by 28.5% . The design in [37] demonstrates a fully folding quadrotor design similar to ours, but it involves the addition of two servomotors just for the attitude control in a stacked bicopters configuration, apart from the servomotor required to modify the configurations. Also, no experimental validation is presented. The design in [38] can fold into a Y-configuration, making the drone of a propeller width on one side. To pass through extremely narrow gaps, first, the head of the drone is folded into a narrow configuration; then, in the middle of the gap, it has to transform into an inverted Y configuration, making the tail of the drone narrow. This requires very coordinated execution of the trajectory and slows down

TABLE I
COMPARISON AMONG EXISTING DESIGNS AND OUR PROPOSED ONE

Design	Falanga et al. [7]	Riviere et al. [16]	Bai et al. [35]	Desbiez et al. [36]	Vundela et al. [37]	Hu et al. [38]	Ours
w_m (%) ↑	36.58*	52.24	15.7*	28.5	53.44*	81.13**	69.13
S_n ↓	4	2	1	1	3	4	1
DOFs ↑	4	0	4	4	4	4	4
Exp.	Yes	Yes	Yes	Yes	No	Yes	Yes

*: no reported size reduction data available, based on deduction from figures
**: only half of the drone reduced to this at a time w_m: Maximum width reduction, S_n: No of servomotors used, DOFs: Controllable degrees of freedom in narrow configuration, Exp: Whether the experimental evaluation was performed, ↑: higher is better, ↓: lower is better.

the process of passing through the narrow gap. The designs that are the closest candidates for passing through a narrow gap are compared in Table I. Compared to these designs, our design reduces the size of the drone by the maximum amount (except design in [38], which does not become fully narrow at a time and uses a step-by-step approach to pass), uses the least number of servomotors to control the configurations or attitude, is controllable in narrow configurations and has been proven effective in experiments. To the best of our knowledge, our design achieves the most size reduction while remaining controllable in any configuration without significantly increasing the hardware complexity.

The rest of this article is organized as follows. Section II illustrates the mechanical design of the MorphoCopter, Section III introduces a moment of inertia and control action-aware controller design for the MorphoCopter. Section IV shows the extensive simulation and experiment-based performance evaluation. Finally, Section V concludes this article. Details about the hardware used are shown in Appendix.

II. HARDWARE DESIGN

A. MorphoCopter(m-n) Nomenclature

We introduce a nomenclature in the form of a MorphoCopter(m-n) for future community use, where m indicates the number of thrust-producing motors and n indicates the number of rigid links. For example, we have constructed MorphoCopter(4-2) with four thrust-producing brushless direct current (BLDC) motors with propellers. These motors are mounted on the ends of two arms, which can rotate with respect to each other via a revolute joint actuated by a servomotor. These arms also have enough vertical offset to allow the top propellers to overlap with the bottom propellers. For simplicity, we will denote MorphoCopter(4-2) as MorphoCopter hereon. Also, motor and propeller words are used interchangeably to represent the BLDC motor-propeller set. Fig. 1 showcases a few out of infinitely many possible configurations of the MorphoCopter. These are just some examples, and the MorphoCopter can be controlled at any angle from $0°$ to $90°$ between arms. In our design, the lower arm also houses a Pixhawk flight controller, an onboard computer Raspberry Pi, a servomotor, and other necessary peripherals. The upper arm only houses the required BLDC motors and electronic speed controllers (ESCs). First, let us define a few geometric notations for MorphoCopter.

This article has been accepted for inclusion in a future issue of this journal. Content is final as presented, with the exception of pagination.

MODI et al.: MORPHOCOPTER: DESIGN, MODELING, AND CONTROL OF A NEW TRANSFORMABLE QUAD–BI COPTER
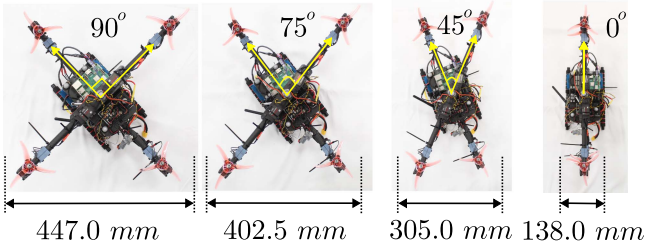
3

Fig. 1. Overview of the MorphoCopter(4-2): where 4 is the number of thrust-producing motors and 2 is the number of rigid links. The figure shows examples of various configurations having different angles between the links and corresponding changes in the width.
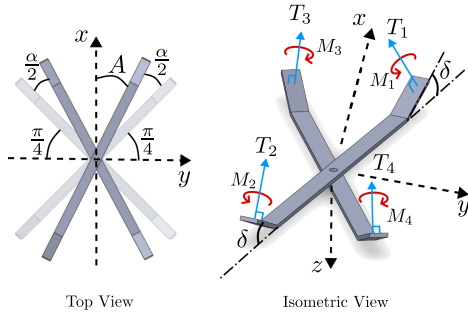

Fig. 2. MorphoCopter geometric notations. Angles α, A, and $\pi/4$ are in the x-y plane. Angle δ is out of the x-y plane.

B. MorphoCopter Geometric Notations

The required notations followed through this article are shown in Fig. 2. We use a front-right-down (FRD) body reference frame. This means the front of the MorphoCopter is the body-attached x-axis, the right of the MorphoCopter is the body-attached y-axis, and downward is the body-attached z-axis. The world reference frame we use is in the north-east-down convention. We define the rotation about the body x-axis as roll, about the body y-axis as pitch, and about the body z-axis as yaw.

In Fig. 2, T_i indicates the thrust force generated by the motor i. M_i indicates the reaction moment generated by the motor i. The joint angle α is defined as the rotation of the upper arm with respect to the lower arm, with $\alpha = 0$ being a standard quadcopter configuration and $\alpha = \pi/2$ being a stacked bicopters configuration. As the upper arm rotates with respect to the lower arm, we consider the body x-axis to always remain at the center of the arms, i.e., when the upper arm rotates with respect to the lower arm, the joint angle α is distributed as $\alpha/2$ on the right-hand side and left-hand side of the MorphoCopter, as shown in Fig. 2. The translucent image in Fig. 2 shows where the arms would be in the standard quadcopter configuration, which is $\pi/4$ radians from both the body x and y axes. Hence, the angle made by the upper arm or lower arm with respect to the body x-axis at any joint angle α will be $(\pi/4 - \alpha/2)$. We will represent this angle as A hereon. The BLDC motors are also tilted inwards by a fixed angle δ, as shown in Fig. 2, for the roll control in an extremely narrow configuration, which is elaborated in Section II-D.
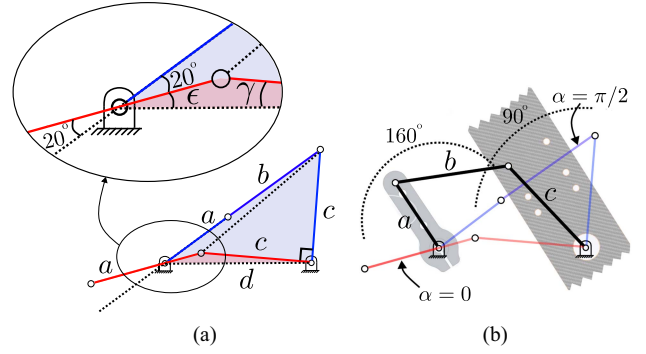

Fig. 3. (a) Geometric synthesis of the four-bar mechanism for upper arm rotation. (b) Constructed four-bar mechanism along with images of servohorn and partial upper arm. Red links correspond to a standard quadcopter configuration ($\alpha = 0$) and blue links correspond to fully folded configuration ($\alpha = \pi/2$).

C. Actuated Rotary Joint

A servomotor controls the rotation of the upper arm of the MorphoCopter through a four-bar linkage mechanism, as shown in Fig. 3. The four-bar linkage parameters are decided considering size constraints, servo motor constraints, and the following requirements to make the hardware robust.

1) The input angle range should be 160°, considering the maximum range of the servomotor being 180°.
2) The output angle range should be 90°.
3) The output should be a rocker link.
4) The mechanism should physically limit the upper arm rotation such that 0° ≤ α ≤ 90° is strictly followed, even if the servomotor malfunctions. $\alpha < 0°$ or $\alpha > 90°$ will essentially alter the motor order, leading to a positive feedback control loop and inevitable crash.

The above-mentioned requirements ensure that the Morpho-Copter does not enter any uncontrollable configuration while maximizing the available leverage of the servomotor torque. We use geometric synthesis to generate a mechanism with the above-mentioned requirements. Fig. 3(a) shows the geometries corresponding to both extremes of the mechanism. Here, a is the servomotor horn, b is a coupler link, c is the distance between the upper arm pivot and the coupler attachment location on the upper arm, and d is the distance between the servomotor axis and the upper arm pivot. The red lines in Fig. 3(a) correspond to the joint angle $\alpha = 0$, and blue lines correspond to the joint angle $\alpha = \pi/2$. The angles ϵ and γ are unknown angles that we will use for forming the equations. Now, using the red highlighted triangle shown in Fig. 3(a), we can form the following equality:

$$\frac{c}{\sin}\epsilon = \frac{b-a}{\sin}\gamma = \frac{d}{\sin(180° - \epsilon - \gamma)}. \tag{1}$$

Using the blue highlighted triangle in Fig. 3(a), we can form the following equality:

$$\frac{c}{\sin}(\epsilon + 20°) = \frac{a+b}{\sin(\gamma + 90°)}$$

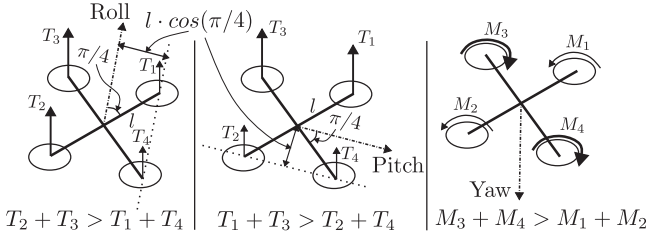$$= \frac{d}{\sin(180° - ((\epsilon + 20°) + (\gamma + 90°)))}. \tag{2}$$

Fig. 4. Standard quadrotor attitude control. Differences in thrusts or reaction moments produced are utilized for roll, pitch, and yaw control.
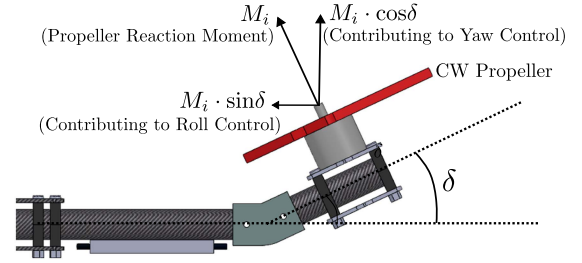

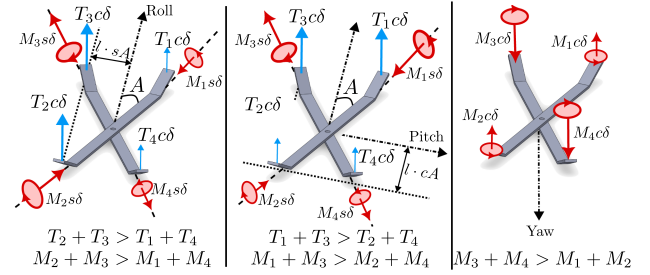Fig. 5. Fixed tilt of motors for roll control for $\alpha > 0$.

Fig. 6. MorphoCopter attitude control. Differences in thrust or reaction moments produced are utilized for roll, pitch, and yaw control. In the figure, $c\delta := \cos(\delta), s\delta := \sin(\delta), sA := \sin(A), cA := \cos(A)$.

This system of equations consists of four equations and six variables. As a is the length of the servomotor horn, we consider it as known (i.e., 24.33 mm in our case). Also, we choose c to be 35 mm as a design choice, considering the feasibility of attaching the coupler to the upper arm. Hence, we solve a system of four nonlinear equations with four unknowns using the trust-region-dogleg algorithm. This numerical solution yields the four-bar mechanism with $a = 24.33$ mm, $b = 35.69$ mm, $c = 35$ mm, and $d = 42.48$ mm. Fig. 3(b) shows this mechanism along with extremes of the mechanism corresponding to $\alpha = 0$ and $\alpha = \pi/2$.

D. MorphoCopter Dynamics-Based Adaptation

The standard *X*-configuration quadcopter utilizes the difference in thrusts or reaction moments of propellers to control the attitude, as shown in Fig. 4. The roll control and pitch control require increasing the total thrust on one side and decreasing it on the other to produce the net moment for the whole body. In the standard configuration, two propellers rotate clockwise, and two propellers rotate counterclockwise. For the yaw control, the speeds of the propellers rotating in the same directions (i.e., clockwise or counterclockwise) are increased or decreased such that the net reaction moment generated contributes toward yaw control. The roll and pitch controls are directly proportional to the distance of the propellers from the center of mass perpendicular to the desired control axis, as indicated by $l \cdot \cos(\pi/4)$ in Fig. 4. We refer the ability of the propeller thrust manipulation to contribute toward roll/pitch control [proportional to $l \cdot \cos(\pi/4)$] as "control action." In a standard quadcopter, this distance is constant, and hence control-action always remains constant. Also, the rate of change of roll/pitch/yaw angles depends on the respective moments of inertia as well, which remains constant in a standard quadcopter. Hence, a properly tuned controller can remain effective throughout the flight in a standard quadcopter.

Now, considering the MorphoCopter design, both the moments of inertia and propeller distances from the center of mass change based on the joint angle. In an extreme folded configuration, in which the MorphoCopter becomes stacked bicopters (i.e., $\alpha = \pi/2$), the distance of propellers from the roll axis becomes 0, and we would completely lose the roll control if the propellers are attached in a standard manner. To address this without increasing the design complexity, we provide a fixed inward tilt (δ) on each motor, as shown in Fig. 5. Due to the tilt δ, the reaction moments generated by the propellers

(responsible for yaw control in a standard quadcopter) have a partial component ($M_i \cdot \sin\delta$) along the roll axis, which can be utilized to control the MorphoCopter. This component along the roll axis increases with increasing tilt angle δ. However, this tilt also reduces the available total upward thrust and yaw control. To determine the required tilt angle δ, we first quantify the moments of inertia and control action of the MorphoCopter.

Using Fig. 2, the moment of inertia along the body *x*-axis (i.e., roll axis), with an angle of A between the body *x*-axis and upper arm (or lower arm) can be given by

$$I_x(A) = (I_{uy} + I_{ly})\sin^2 A + (I_{ux} + I_{lx})\cos^2 A \qquad (3)$$

where I_{uy} is the moment of inertia of the upper arm along the axis perpendicular to its length and passing through the joint angle pivot. I_{ux} is the moment of inertia of the upper arm along the axis parallel to its length and passing through the joint angle pivot. Similarly, I_{ly} and I_{lx} are the analogous moments of inertia for the lower arm. For simulations and experiments in this article, we derive these values from the computer-aided design (CAD) model of the MorphoCopter by entering material details in the CAD software as accurately as possible. Similarly, the moment of inertia along the body *y*-axis (i.e., pitch axis) can be given by

$$I_y(A) = (I_{uy} + I_{ly})\cos^2 A + (I_{ux} + I_{lx})\sin^2 A. \qquad (4)$$

Fig. 6 illustrates the high-level attitude control schematic for MorphoCopter. The reaction moments from the propellers have increased contribution in roll control as α increases (A decreases). Using Fig. 6, the magnitude of the moment generated along the body *x*-axis (roll axis) by any propeller is given by

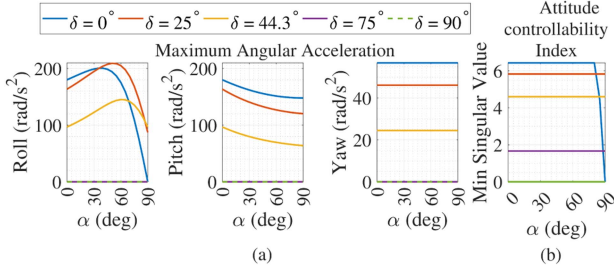$$\tau_x(A) = T_i\cos(\delta)(l\sin A) + M_i\sin(\delta)\cos A \qquad (5)$$

This article has been accepted for inclusion in a future issue of this journal. Content is final as presented, with the exception of pagination.

MODI et al.: MORPHOCOPTER: DESIGN, MODELING, AND CONTROL OF A NEW TRANSFORMABLE QUAD–BI COPTER   5

Fig. 7. (a) Angular acceleration bounds at hover thrust (mg) for our specific design at various (α) and (δ) for roll, pitch, and yaw. (b) Attitude controllability matrix: minimum singular value indicates how close the system is to losing controllability; the higher the minimum singular value, the farther the system is from losing controllability.

Fig. 8. Cascaded controller.

and the magnitude of the moment generated along the pitch axis by a single propeller is given by

$$\tau_y(A) = T_i\cos(\delta)(l\cos A) - M_i\sin(\delta)\sin A \qquad (6)$$

where M_i is the reaction moment and T_i is the total thrust generated by propeller i. M_i is related to T_i by a moment coefficient [39] K_m defined as

$$M_i = K_m \cdot T_i \approx K_m \cdot \frac{T_{\text{body}}}{4}. \qquad (7)$$

T_{body} is the total thrust generated by all the propellers. We will refer T_{body} as T for concise representation.

Using $I_x(A)$, $I_y(A)$, $T_x(A)$, and $T_y(A)$ derived here, we determine the required inward tilt (δ) of the propellers. If we want to achieve the same body roll rate at joint angles $\alpha = \pi/2$ (i.e., $A = 0$) and $\alpha = 0$ (i.e., $A = \pi/4$), then we need

$$\frac{\tau_x(A=0)}{I_x(A=0)} = \frac{\tau_x(A=\pi/4)}{I_x(A=\pi/4)}. \qquad (8)$$

Using (3), (5), and (7), we get

$$\frac{K_m\frac{T}{4}\cdot\sin(\delta)}{(I_{ux}+I_{lx})} = \sqrt{2}\cdot\frac{\frac{T}{4}\cos(\delta)l + K_m\frac{T}{4}\cdot\sin(\delta)}{(I_{uy}+I_{ly})+(I_{ux}+I_{lx})}. \qquad (9)$$

Solving this equation for δ with parameters shown in Table IV, we get $\delta = 44.30°$. However, at this tilt, the upward component of the total thrust generated from each motor (as well as the component of the reaction moment contributing to yaw control) will only be $\cos(44.30°) \approx 71.57\%$, reducing the efficiency of the MorphoCopter significantly. So, we decide that we only need half of the maneuverability about the roll axis at the configuration with $A = 0$. With this, the required tilt will be calculated using

$$\frac{\tau_x(A=0)}{I_x(A=0)} = \frac{\tau_x(A=\pi/4)}{2\cdot I_x(A=\pi/4)}. \qquad (10)$$

Solving this equation, we get $\delta = 23.49°$. For ease of manufacturability, we round off the tilt angle to $25°$. At this tilt, we still have $\cos(25°) \approx 90.63\%$ of the total thrust generated in the upward direction and $\approx 90.63\%$ of the reaction moment generated contributing toward yaw control.

Fig. 7 explores the controllability aspect of the design at various joint angles (α) and tilt angles (δ). First thre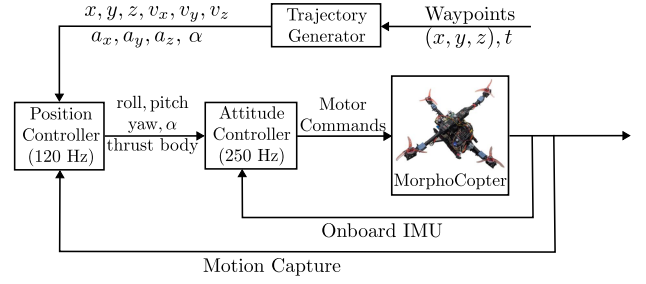e figures show the maximum angular acceleration in each direction while maintaining hover thrust (mg) in the upward direction in a world frame. We can observe that with $\delta = 0°$, the drone would produce 0 roll acceleration for $\alpha = 90°$ and would loose the controllability. With just $\delta = 25°$, it is able to maintain the roll control throughout the α range, with almost half the angular acceleration capability at $\alpha = 90°$. In pitch and yaw direction, $\delta = 25°$ does not cause much loss in the control authority. The last plot in Fig. 7 shows the minimum singular value of the attitude controllability matrix, indicating how close the system is to losing the controllability. We can see that with $\delta = 0°$, the MorphoCopter would lose the controllability for $\alpha > 80°$. Due to the dependency of the moments of inertia and the body moment generation on the joint angle, as illustrated in (3)–(6), it is necessary to design an adaptive controller that considers these factors, which we will discuss next.

III. CONTROLLER FRAMEWORK

The current baseline controller is a nonlinear PID controller implemented in a cascaded format, as shown in Fig. 8. The waypoints and the desired time to reach those waypoints are provided to the trajectory generator. The trajectory generator generates desired position, velocity, acceleration, and joint angle commands using these waypoints. The trajectory generator currently generates a minimum-snap trajectory of the fifth-order polynomial for x, y, and z, while the joint angle α is manually scripted into the trajectory in the current implementation. Based on these desired values, the position controller calculates the difference between the desired values and the actual values estimated by the motion capture cameras and generates the desired attitude command for the attitude controller. The attitude controller calculates the difference between the desired attitude and the estimated attitude by onboard inertial measurement unit (IMU) sensors and calculates the commands for each of the motors. We will explore these controllers in more detail in the upcoming sections. This baseline controller is an adaptation of the controller formulated in [40] according to the MorphoCopter varying dynamics.

A. Position Controller

As shown in Fig. 8, the position controller takes the desired position, velocity, acceleration, and joint angles as input from the trajectory generator and compares them with motion capture camera-based estimated position and velocity. We calculate error in positions $\mathbf{e_p}$, error in velocity $\mathbf{e_v}$, and integral error $\mathbf{e_i}$. Using

these, we can generate the desired force vector $\mathbf{f_{des}}$ using

$$\mathbf{f_{des}} = m \cdot \left(\mathbf{a_{des}} + [0,0,-g]^T + \mathbf{k_p e_p} + \mathbf{k_v e_v} + \mathbf{k_i e_i}\right) \tag{11}$$

where m is the mass of the MorphoCopter, $\mathbf{a_{des}}$ is the desired acceleration as per the trajectory generator, g is the gravitational constant, and $\mathbf{k_p}$, $\mathbf{k_v}$, and $\mathbf{k_i}$ are position controller gain matrices. Using $\mathbf{f_{des}}$, we can calculate desired body z-axis ($\mathbf{z_{b,des}}$) in FRD convention as

$$\mathbf{z_{b,des}} = \frac{-\mathbf{f_{des}}}{||\mathbf{f_{des}}||}. \tag{12}$$

The intermediate body x-axis ($\mathbf{x_{c,des}}$) based on desired yaw angle is calculated using

$$\mathbf{x_{c,des}} = [\cos(\psi_{des}), \sin(\psi_{des}), 0]^T. \tag{13}$$

With these, we can determine the desired body y-axis ($\mathbf{y_{b,des}}$) and desired body x-axis ($\mathbf{x_{b,des}}$) as

$$\mathbf{y_{b,des}} = \frac{\mathbf{z_{b,des}} \times \mathbf{x_{c,des}}}{||\mathbf{z_{b,des}} \times \mathbf{x_{c,des}}||} \tag{14}$$

$$\mathbf{x_{b,des}} = \mathbf{y_{b,des}} \times \mathbf{z_{b,des}}. \tag{15}$$

Using $\mathbf{x_{b,des}}$, $\mathbf{y_{b,des}}$, and $\mathbf{z_{b,des}}$, the desired body rotation matrix with respect to the world frame can be determined using

$$\mathbf{R_{des}} = [\mathbf{x_{b,des}}, \mathbf{y_{b,des}}, \mathbf{z_{b,des}}]. \tag{16}$$

We use this desired rotation matrix and compare it with the estimated rotation matrix in the attitude controller to generate desired motor commands, as explained next.

B. Adaptive Attitude Controller

Based on the IMU readings, the estimated rotation matrix of the IMU sensor with respect to the world frame is given by

$$\mathbf{R_{IMU}} = [\mathbf{x_b}, \mathbf{y_b}, \mathbf{z_b}]. \tag{17}$$

As shown in Fig. 2, as we consider the body x-axis to always remain in the middle of the arms, the body x-axis and IMU sensor (housed in the lower arm) will be at angle $\alpha/2$ with respect to each other. Therefore, the rotation matrix estimated by the IMU sensor needs to be transformed into a MorphoCopter frame of reference using

$$\mathbf{R} = \begin{bmatrix} \cos(\alpha/2) & \sin(\alpha/2) & 0 \\ -\sin(\alpha/2) & \cos(\alpha/2) & 0 \\ 0 & 0 & 1 \end{bmatrix} \cdot \mathbf{R_{IMU}}. \tag{18}$$

Using this estimated rotation matrix and the desired rotation matrix from (16), we calculate the error in the attitude of the MorphoCopter using a vee map

$$\mathbf{e_R} = \frac{1}{2} \left(\mathbf{R_{des}R}^T - \mathbf{R}^T\mathbf{R_{des}}\right)^V. \tag{19}$$

Using $\mathbf{e_R}$, we can generate integral rotational error using

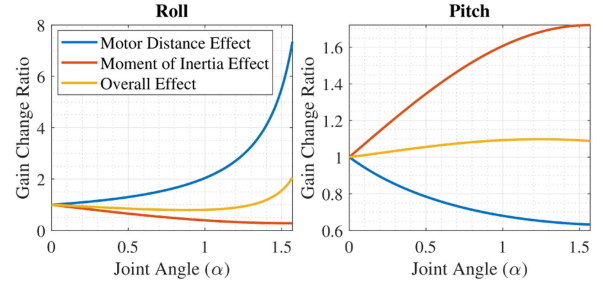$$\mathbf{e_{R,int}} = \int_0^t \mathbf{e_R} \, dt. \tag{20}$$

Fig. 9.   Adaptive gain tuning due to change in motor distance and change in moments of inertia in roll and pitch directions.

To dampen the rotation, we consider the desired angular velocity to be zero, and hence the error in the angular velocity is

$$\mathbf{e_W} = -\boldsymbol{\omega} \tag{21}$$

where $\boldsymbol{\omega}$ is the estimated angular velocity by the IMU sensor and then transformed to the MorphoCopter body frame using

$$\boldsymbol{\omega} = \begin{bmatrix} \cos(\alpha/2) & -\sin(\alpha/2) & 0 \\ \sin(\alpha/2) & \cos(\alpha/2) & 0 \\ 0 & 0 & 1 \end{bmatrix} \boldsymbol{\omega}_{IMU}. \tag{22}$$

Now, using $\mathbf{e_R}$, $\mathbf{e_{R,int}}$, and $\mathbf{e_W}$, we calculate intermediate desired torque in the body reference frame as follows:

$$\boldsymbol{\tau}'_{des} = \mathbf{k_{p,inner} e_R} + \mathbf{k_{v,inner} e_W} + \mathbf{k_{i,inner} e_{R,int}} \tag{23}$$

where $\mathbf{k_{p,inner}}$, $\mathbf{k_{v,inner}}$, and $\mathbf{k_{i,inner}}$ are the attitude controller gain matrices tuned at $\alpha = 0$. We can determine the desired collective thrust to be generated by all the motors using

$$T = \mathbf{f_{des}} \cdot \mathbf{z_b}. \tag{24}$$

Up to this point, the controller is unaware of the variable moments of inertia and control action of the MorphoCopter. Using the moments of inertia and effective body moments determined in (3)–(6), the final desired body torque can be calculated from (23) as

$$\boldsymbol{\tau}_{des} = \begin{bmatrix} \frac{I_x(A)}{I_x(0)} \cdot \frac{\tau_x(0)}{\tau_x(A)} & 0 & 0 \\ 0 & \frac{I_y(A)}{I_y(0)} \cdot \frac{\tau_y(0)}{\tau_y(A)} & 0 \\ 0 & 0 & 1 \end{bmatrix} \boldsymbol{\tau}'_{des}. \tag{25}$$

This final desired torque (25) and desired thrust (24) are sent to the onboard Pixhawk controller running PX4 firmware via its offboard control mode, which then uses its mixing to send the pulsewidth-modulated commands to the BLDC motors.

The ratios in (25) essentially change the overall gain multiplier of the attitude PID controller (23) adaptively based on the joint angle α. This makes our attitude controller essentially a gain-scheduled adaptive controller. For the prototype of the Morpho-Copter we constructed, the base gains corresponding to $\alpha = 0$ are tuned with trial and error in the simulation environment described later in this article. The ratios in (25) affect the attitude controller gains, as shown in Fig. 9. We can see that in the roll direction, as the joint angle α approaches $\pi/2$, due to propellers and motors coming close to the roll axis, we need to effectively increase the gains by a large amount. However, this decreased

motor distance also decreases the moment of inertia about the roll axis. Hence, overall, the gains at $\alpha = \pi/2$ need to be around double the gain at $\alpha = 0$. Also, at some intermediate joint angles (e.g., $\alpha = 0.78$), the gains needed in the roll direction are 0.75 times the gains needed at $\alpha = 0$. This makes the MorphoCopter more agile in roll direction at those joint angles. Similarly, in the pitch direction, the moment of inertia increases as α approaches $\pi/2$, but at the same time, control action also increases due to the increased distance between the pitch axis and the propellers. Hence, the overall controller gains remain almost constant in pitch direction for all joint angles.

Next, we will explore the simulations and experiments performed to validate the novel MorphoCopter design and the adaptive controller.

IV. SIMULATIONS AND EXPERIMENTS

The simulation was designed in the Gazebo simulator via PX4 software using the accurate CAD model of the hardware. All the evaluations were first done in the simulator to verify the controller, and then were performed on the hardware in the form of experiments. We primarily performed five kinds of evaluations at various joint angles: A. Hover performance analysis B. External perturbation inputs C. Performance in a shape 8 trajectory D. Performance in a diamond shape trajectory E. Passing through an environment with very narrow gaps. Considering the page limitations and to reduce repetitive details, we show simulation results only for the most complex scenarios, while we will show experiment results for all the evaluations. The experiments are also summarized in a video in the supplementary material.

A. Hover Performance in Experiments

To compare the MorphoCopter's hover performance in standard X configuration ($\alpha = 0$) and fully folded stacked bicopters configuration ($\alpha = \pi/2$), experiments with MorphoCopter hovering at the same location ($x = 0$ m, $y = 0$ m, $z = -1.2$ m) were conducted starting with the fully charged battery till the minimum specified battery voltage was reached. The experiments were performed with a 4S 3300 mAh LiPo battery. Without folding, in a standard X configuration, the MorphoCopter could hover for 200.75 s. With a fully folded stacked bicopters configuration ($\alpha = \pi/2$), it could hover for 171.56 s. Hence, the MorphoCopter could retain almost 85% hover duration in a fully folded configuration compared to the standard quadcopter configuration.

Fig. 10 shows the hover performance of the MorphoCopter in a histogram format. The figure on the left represents tracking errors in X–Y directions in the form of root-mean-squared errors (RMSEs). This plot also shows the cumulative probability of hovering within various RMSE values using the right axis. The plot on the right shows the histogram of the tracking errors in the Z-direction. These plots indicate how well the MorphoCopter can hover close to the desired location. For both configurations, the hover performance is not much different. The cumulative probability plot in the X–Y direction shows that the probability of the MorphoCopter being within 0.1 m RMSE is 0.90 for a standard quadcopter configuration, which is 0.82 for a fully
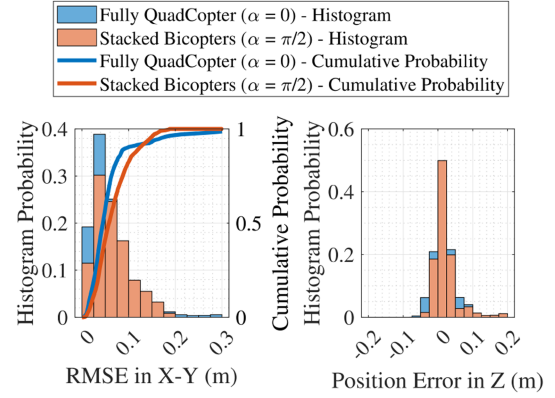

Fig. 10. Probability of MorphoCopter hovering within various distances from the desired hover location in experiments.
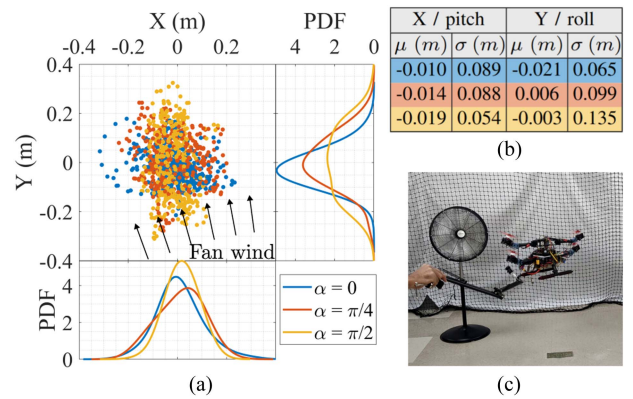

Fig. 11. Test of the robustness with manual perturbation and fan winds. (a) Datapoints of multiple flights at various joint angles along with PDF. (b) PDF mean (μ) and standard deviation (σ) values. (c) Snapshot from the experiment video.

folded stacked bicopters configuration. These plots indicate no significant degradation of hover performance due to the folding of the MorphoCopter.

B. Performance With External Perturbations and Disturbances

In this experiment, the MorphoCopter was asked to hover in the same location while subject to changing high winds from a large fan and manually perturbed by a rod. The snapshot from the test video is shown in Fig. 11(c). The fan was kept on the oscillation mode to keep the winds varying with time. Fig. 11(a) shows the data points of the MorphoCopter location in the X–Y plane during the perturbation test, along with the probability density function (PDF). Fig. 11(b) shows the mean and standard deviation values for the derived PDF. The MorphoCopter was able to maintain the hover location mostly within 0.2 m distance from the target hover location in any configuration. This evaluation can be better visualized in the supplementary video.

The tests we performed in the experiment qualitatively show the robustness of the design with the hardware. We quantify this robustness and test the limits of our design in the simulations by

TABLE II
PERTURBATION LIMIT TEST

	Direction	$\alpha = 0$	$\alpha = 0.6$	$\alpha = 1.1$	$\alpha = \pi/2$
Settling time (s)	x/Pitch	2.0466	2.1567	1.8529	1.9965
	y/Roll	1.9201	1.9891	1.9735	2.0660
Max. force (N)	x/Pitch	59	60	60	62
	y/Roll	59	56	43	39

TABLE III
TRAJECTORY FOLLOWING QUANTITATIVE ANALYSIS

α / Exp. No	RMSE (xy)	RMSE (z)	Maximum error (xy)	Maximum error (z)
Shape 8 trajectory				
$\alpha = 0$	0.047	0.022	0.142	0.069
$\alpha = \pi/4$	0.065	0.024	0.194	0.059
$\alpha = \pi/2$	0.113	0.046	0.228	0.155
Diamond trajectory				
$\alpha = 0$	0.090	0.020	0.199	0.064
$\alpha = 1$	0.111	0.022	0.234	0.060
$\alpha = \pi/2$	0.117	0.045	0.241	0.159
Gap passing experiments				
Exp. 1	0.084	0.053	0.232	0.205
Exp. 2	0.083	0.046	0.197	0.162
Exp. 3	0.086	0.087	0.167	0.277

All numbers are in m.

(a)   (b)
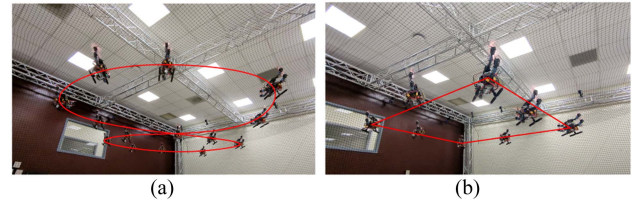
Fig. 13. Snapshots from trajectory traverse with $\alpha = \pi/2$. (a) Shape 8 trajectory. (b) Diamond trajectory.

Fig. 12. Shape 8 and diamond trajectory at various joint angles in experiments. (a) Shape 8 trajectory. (b) Diamond trajectory.

giving quantifiable perturbations. Table II shows the 5% settling time for the perturbation force of 10 N exerted for 1 s duration. The table also indicates the maximum force we are able to apply before the MorphoCopter loses stability. We can see that the maximum force that can be applied to the MorphoCopter in the pitch direction marginally increases with increasing α. While in the roll direction, this maximum force reduces significantly in the fully folded configuration compared to the standard quadrotor configuration. This is expected as the δ is chosen such that the MorphoCopter only has half the control authority in roll direction at the fully folded configuration compared to the standard configuration (see Section II-D). The settling time is not affected much by the joint angle due to the adaptive controller designed in Section III-B.

C. Performance in a Shape 8 Trajectory in Experiments

To verify the controllability of the MorphoCopter in complex maneuvers, the experiments with the shape 8 trajectory were performed at various joint angles. This trajectory was a constant altitude (i.e., −1.2 m) with X-Y trajectory in shape 8, as shown in Fig. 12(a). We performed the experiments with joint angles $\alpha = 0$, $\alpha = \pi/4$, and $\alpha = \pi/2$. As shown in Fig. 12(a), the MorphoCopter is able to follow this complex trajectory well in all the configurations. Please note that the data are trimmed to only show the trajectory traverse duration. In the z-direction plot in Fig. 12(a), we see that the altitude of the MorphoCopter

is around −1m initially instead of −1.2m. This is due to a reduction in thrust just after folding to a higher joint angle with propellers overlapping each other. This drop is temporary, and the MorphoCopter quickly achieves the desired altitude as the integral error kicks in. Table III shows the quantitative performance matrix for this trajectory for all three joint angles. As expected, the MorphoCopter has more errors with higher joint angles, but we believe these larger errors are within the acceptable range.

Fig. 13(a) shows the snapshots of the MorphoCopter traversing this shape 8 trajectories in the fully folded ultranarrow configuration of $\alpha = \pi/2$. At this joint angle, the distance between the propellers and the roll axis is 0. Hence, there is no standard distance-based leverage available for the roll control. This verifies that the propellers' reaction moment is able to control the roll using the fixed inward tilt of the propellers and our adaptive controller design.

D. Performance in a Diamond Shape Trajectory in Experiments

To further verify the controllability of the MorphoCopter in complex maneuvers, the experiments with a diamond-shaped trajectory were performed at various joint angles. The trajectory was a constant altitude (i.e., −1.2 m) with X-Y trajectory in a diamond shape, as shown in Fig. 12(b). The experiments were conducted with joint angles $\alpha = 0, \alpha = 1$, and $\alpha = \pi/2$. This trajectory involves some sharp corners, which the MorphoCopter is able to traverse in a fully folded configuration as well. Similar to the shape-8 trajectory, we observe an initial drop in altitude for $\alpha = \pi/2$, which is quickly corrected by the
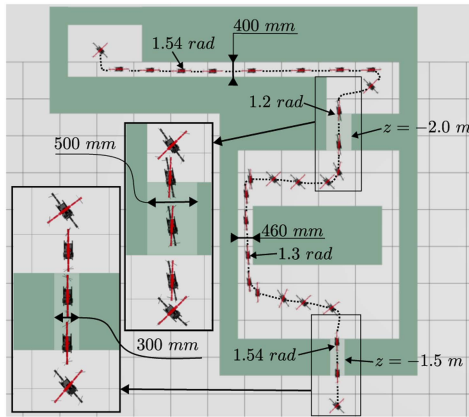
Fig. 14. Morphing sequence for passing through an environment with multiple narrow passages.

Fig. 15. Trajectory the MorhpoCopter followed while traversing the simulation environment.

controller as shown in the z-direction plot in Fig. 12(b). Table III also shows the similar performance for all joint angles.

Fig. 13(b) shows the snapshots of the MorphoCopter traversing this diamond-shaped trajectory in a fully folded ultranarrow configuration of $\alpha = \pi/2$. At this joint angle, again, it verifies the roll control using the propellers' reaction moment and our adaptive controller design.

E. Passing Through an Environment With Very Narrow Gaps

1) Simulation: First, we show the results from the simulation in a complex scenario containing multiple narrow gaps. Fig. 14 shows the environment created for evaluating the performance of the MorphoCopter. The environment contains multiple narrow passages, with the narrowest passage of 300 mm. The environment also contains walls that require the MorphoCopter to take multiple turns and change the heading directions. As shown in Fig. 1, the width of the MorphoCopter in a standard quadcopter configuration is 447 mm, which is larger than the narrow gaps present in the environment. Hence, even with a very precise controller, the standard quadcopter cannot access such an environment.

We design a minimum snap trajectory to pass through this environment, which involves multiple joint angle manipulations. Currently, the waypoints for the trajectory are determined manually. Fig. 14 shows the trajectory followed by the MorphoCopter to pass through this environment, along with a close-up look at the morphing sequences for passing through narrow gaps. The dotted line refers to the trajectory in 3-D space. Fig. 15 shows the desired and actual trajectories in the time domain. We see that the MorphoCopter can change its configuration to various joint angles on the fly while passing through the environment. We are able to leverage the unique feature of the design by morphing the MorphoCopter only up to the desired angle without losing controllability.

We also perform several simulations with different types of narrow passages to demonstrate the robustness of the design in navigating complex environments. Fig. 16 shows the simulation trajectories with such narrow passages. The figures show section
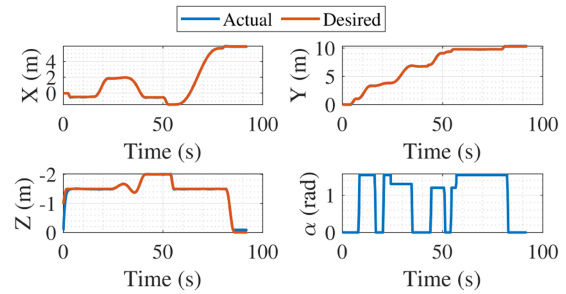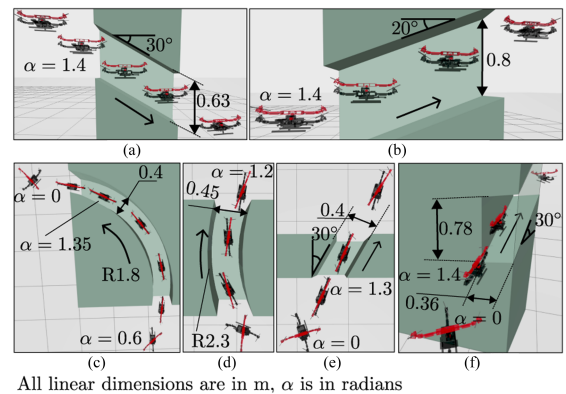

Fig. 16. Various types of narrow passages in simulations. The snapshots are taken with a section view of the obstacles for better visibility. (a) 0.3 m wide and 0.63 m tall passage with a downward slope of 30°. (b) 0.3 m wide and 0.8m tall passage with an upward slope of 20°. (c) 0.4 m wide passage forming a quarter-circle of 1.8 m radius in horizontal plane. (d) 0.45 m wide passage forming an arc of 2.3 m radius in horizontal plane. (e) 0.4 m wide passage inclined in horizontal plane with 30°. (f) 0.36 m wide and 0.78 m tall passage inclinded both in horizontal and vertical plane with 30°.
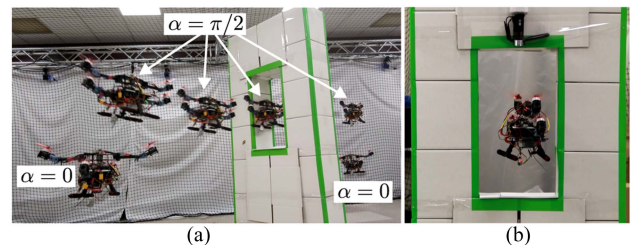

Fig. 17. Snapshots from the video of the MorphoCopter passing through a narrow gap. (a) Isometric view with snapshots taken at certain time intervals. (b) Front view while the MorphoCopter is inside the narrow passage.

cutouts of the environment for better visibility. Environment (a) and (b) have slopes of 30° and 20° respectively, each of them having a different depth of the passage. Environment (c) has a quarter-circle passage in the horizontal plane, and the MorphoCopter needs to constantly change the yaw to navigate through this environment in a very narrow configuration. Environment (d) has a similar horizontal curved passage. Environment (e) has a slanted, narrow passage in the horizontal plane. Environment (f) has slopes in both vertical and horizontal planes.
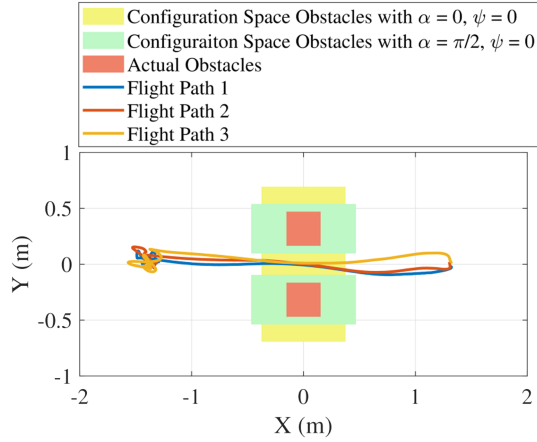
Fig. 18.   Trajectory followed by the MorphoCopter to pass through the narrow gap at $\alpha = \pi/2$ along with configuration space obstacle representation at various joint angles.
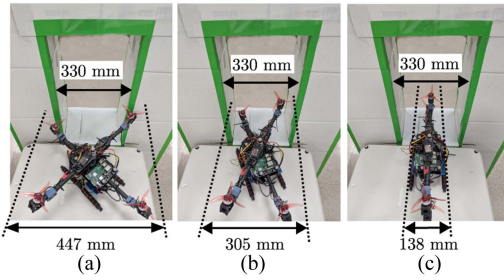

Fig. 19.   Visualization of MorphoCopter size at various joint angles against a narrow passage. (a) $\alpha = 0$. (b) $\alpha = \pi/4$. (c) $\alpha = \pi/2$.

2) Experiments: As shown in Fig. 17, a narrow passage was created using some obstacles. Due to space constraints, we test the performance of the MorphoCopter for a single narrow passage of 330 mm width.

The difficulty of the standard quadcopter in passing through this narrow gap can be better visualized in the configuration space plot shown in Fig. 18 and 3-D space figures in Fig. 19. The plot shows the obstacles in an *X-Y* 2-D plane with a red color. Considering the width of the MorphoCopter in standard *X* configuration ($\alpha = 0$), the configuration space obstacles are shown in yellow. As both obstacles are merged in the configuration space with $\alpha = 0$, the MorphoCopter cannot pass through them in a standard quadcopter configuration. The green boxes show the configuration space obstacle with the joint angle of $\pi/2$ rad. Folding the MorphoCopter to this joint angle creates a passage of 166 mm width for the MorphoCopter to pass through safely, leaving some room for errors in trajectory tracking. The actual paths followed by the MorphoCopter in three different experiments are shown in Fig. 18 and the quantitative performance is shown in Table III.

Fig. 20 shows the *X*-, *Y*-, and *Z*-direction desired and actual trajectories for the MorphoCopter in the gap passing experiment. The black vertical line indicates the time when the Morpho-Copter was commanded to fold from a standard quadcopter configuration to the fully folded bicopter configuration. Even with the narrow configuration after folding, it is able to track trajectories very well.
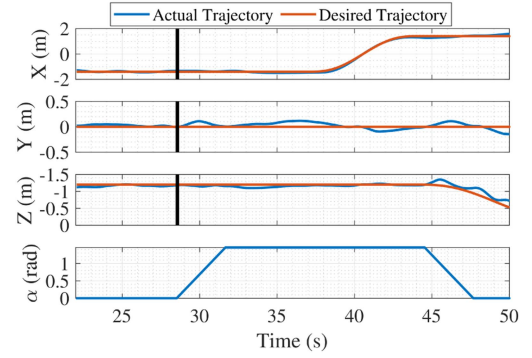

Fig. 20.   Trajectory of the MorphoCopter followed while passing through a narrow gap in an experiment. The vertical black line indicates the time when the MorphoCopter was commanded to fold.

V. CONCLUSION

In this article, we presented hardware design, adaptive controller, and experimental verification of the novel folding drone—MorphoCopter(4-2). We showcase that our simplistic design can reduce the size by the maximum amount of any available similar designs while still being controllable in all configurations. We verified the controllability of the MorphoCopter in any configuration through rigorous experiments and also showcased the ability to morph into a very narrow configuration, pass through a very narrow passage, and then come back to the standard configuration on the fly. Our current specific prototype has a limited flying duration and payload capacity, which we would like to improve in further iterations. Also, we will delve into designing optimum path planning and trajectory planning algorithms to autonomously generate the desired joint angle α and to leverage the capabilities of this novel MorphoCopter design.

APPENDIX
HARDWARE DETAILS

TABLE IV
MORPHOCOPTER(4-2) CURRENT DESIGN HARDWARE DETAILS

| Hardware parameters	
mass (m)	1.8 kg
Propeller to C.O.M. distance (l)	218.21 mm
I_{ux}	1.80×10^{-3} kg m^2
I_{uy}	11.72×10^{-3} kg m^2
I_{lx}	2.42×10^{-3} kg m^2
I_{ly}	14.29×10^{-3} kg m^2
K_m	0.055 Nm/N
Motors	T Motor 2207 - 2500 KV
ESCs	T Motor Air - 40 A
Propellers	T Motor - 4943 tri-blade
Battery	HRB 3300 mAh - 4S LiPo 60C
Position gains	
[P, I, D] gains for x/y	[1.4, 1.4, 0.2]
[P, I, D] gains for z	[5.0, 4.5, 0.75]
Attitude gains	
[P, I, D] gains for roll/pitch	[0.5, 0.075, 0.004]
[P, I, D] gains for yaw	[0.2, 0.1, 0.004]

C.O.M: Center of mass.

REFERENCES

[1] C. Yuan, Z. Liu, and Y. Zhang, "Fire detection using infrared images for UAV-based forest fire surveillance," in *Proc. Int. Conf. Unmanned Aircr. Syst.*, Miami, FL, USA, 2017, pp. 567–5721, doi: 10.1109/ICUAS.2017.7991306.

[2] J. Dong, K. Ota, and M. Dong, "UAV-based real-time survivor detection system in post-disaster search and rescue operations," *IEEE J. Miniaturization Air Space Syst.*, vol. 2, no. 4, pp. 209–219, Dec. 2021, doi: 10.1109/JMASS.2021.3083659.

[3] E. Ackerman and M. Koziol, "The blood is here: Zipline's medical delivery drones are changing the game in Rwanda," *IEEE Spectr.*, vol. 56, no. 5, pp. 24–31, May 2019, doi: 10.1109/MSPEC.2019.8701196.

[4] D. Falanga, E. Mueggler, M. Faessler, and D. Scaramuzza, "Aggressive quadrotor flight through narrow gaps with onboard sensing and computing using active vision," in *Proc. IEEE Int. Conf. Robot. Automat.*, Singapore, 2017, pp. 5774–5781, doi: 10.1109/ICRA.2017.7989679.

[5] Z. Liu and L. Cai, "Simultaneous planning and execution for quadrotors flying through a narrow gap under disturbance," *IEEE Trans. Control Syst. Technol.*, vol. 31, no. 6, pp. 2644–2659, Nov. 2023, doi: 10.1109/TCST.2023.3283446.

[6] J. Lin, L. Wang, F. Gao, S. Shen, and F. Zhang, "Flying through a narrow gap using neural network: An end-to-end planning and control approach," in *Proc. IEEE/RSJ Int. Conf. Intell. Robots Syst.*, Macau, China, 2019, pp. 3526–3533, doi: 10.1109/IROS40897.2019.8967944.

[7] D. Falanga, K. Kleber, S. Mintchev, D. Floreano, and D. Scaramuzza, "The foldable drone: A morphing quadrotor that can squeeze and fly," *IEEE Robot. Automat. Lett.*, vol. 4, no. 2, pp. 209–216, Apr. 2019, doi: 10.1109/LRA.2018.2885575.

[8] S. H. Derrouaoui, Y. Bouzid, M. Guiatni, I. Dib, and N. Moudjari, "Design and modeling ofunconventional quadrotors," in *Proc. 28th Mediterranean Conf. Control Automat.*, Saint-Raphaël, France, 2020, pp. 721–726, doi: 10.1109/MED48518.2020.9183002.

[9] J. M. Butt, X. Ma, X. Chu, and K. W. Samuel Au, "Adaptive flight stabilization framework for a planar 4R-foldable quadrotor: Utilizing morphing to navigate in confined environments," in *Proc. Amer. Control Conf.*, Atlanta, GA, USA, 2022, pp. 1–7, doi: 10.23919/ACC53348.2022.9867402.

[10] G. Cui, R. Xia, X. Jin, and Y. Tang, "Motion planning and control of a morphing quadrotor in restricted scenarios," *IEEE Robot. Automat. Lett.*, vol. 9, no. 6, pp. 5759–5766, Jun. 2024, doi: 10.1109/LRA.2024.3396109.

[11] S. H. Derrouaoui et al., "Trajectory tracking control of a morphing UAV using radial basis function artificial neural network based fast terminal sliding mode: Theory and experimental," *Aerosp. Sci. Technol.*, vol. 155, Dec. 2024, Art. no. 109719, doi: 10.1016/j.ast.2024.109719.

[12] S. H. Derrouaoui, M. Guiatni, Y. Bouzid, I. Dib, and N. Moudjari, "Dynamic modeling of a transformable quadrotor," in *Proc. Int. Conf. Unmanned Aircr. Syst.*, Athens, Greece, 2020, pp. 1714–1719, doi: 10.1109/ICUAS48674.2020.9213908.

[13] Y. Bouzid, S. H. Derrouaoui, and M. Guiatni, "PID gain scheduling for 3D trajectory tracking of a quadrotor with rotating and extendable arms," in *Proc. Int. Conf. Recent Adv. Math. Informat.*, Tebessa, Algeria, 2021, pp. 1–4, doi: 10.1109/ICRAMI52622.2021.9585973.

[14] A. Aikebaier, Q. Wang, Y. Bai, and Q. Wang, "Motion configuration planning method of morphing quadrotor," in *Proc. IEEE Int. Conf. Unmanned Syst.*, Nanjing, China, 2024, pp. 1597–1602, doi: 10.1109/ICUS61736.2024.10839796.

[15] C. Kim, H. Lee, M. Jeong, and H. Myung, "A morphing quadrotor that can optimize morphology for transportation," in *Proc. IEEE/RSJ Int. Conf. Intell. Robots Syst.*, Prague, Czech Republic, 2021, pp. 9683–9689, doi: 10.1109/IROS51168.2021.9636558.

[16] V. Riviere, A. Manecy, and S. Viollet, "Agile robotic fliers: A morphing-based approach," *Soft Robot.*, vol. 5, no. 5, pp. 541–553, 2018, doi: 10.1089/soro.2017.0120.

[17] S. Li, F. Liu, Y. Gao, J. Xiang, Z. Tu, and D. Li, "AirTwins: Modular bi-copters capable of splitting from their combined quadcopter in midair," *IEEE Robot. Automat. Lett.*, vol. 8, no. 9, pp. 6068–6075, Sep. 2023, doi: 10.1109/LRA.2023.3301776.

[18] A. Fabris, S. Kirchgeorg, and S. Mintchev, "A soft drone with multimodal mobility for the exploration of confined spaces," in *Proc. IEEE Int. Symp. Safety, Security, Rescue Robot.*, New York City, NY, USA, 2021, pp. 48–54, doi: 10.1109/SSRR53300.2021.9597683.

[19] A. Fabris, E. Aucone, and S. Mintchev, "Crash 2 squash: An autonomous drone for the traversal of narrow passageways," *Adv. Intell. Syst.*, vol. 4, no. 11, 2022, Art. no. 2200113.

[20] N. Bucki and M. W. Mueller, "Design and control of a passively morphing quadcopter," in *Proc. Int. Conf. Robot. Automat.*, Montreal, QC, Canada, 2019, pp. 9116–9122, doi: 10.1109/ICRA.2019.8794373.

[21] H. Jia, S. Bai, and P. Chirarattananon, "Aerial manipulation via modular quadrotors with passively foldable airframes," *IEEE/ASME Trans. Mechatron.*, vol. 28, no. 4, pp. 1930–1938, Aug. 2023, doi: 10.1109/TMECH.2023.3275143.

[22] Y. Wang, C. Liu, and K. Zhang, "A novel morphing quadrotor UAV with Sarrus-linkage-based reconfigurable frame," in *Proc. 6th Int. Conf. Reconfigurable Mechanisms Robots*, Chicago, IL, USA, 2024, pp. 283–289, doi: 10.1109/ReMAR61031.2024.10619988.

[23] X. Wu, J. Du, C. Hu, K. Ma, B. Li, and F. Xu, "Design and implementation of flexible deformable special flying robot," in *Proc. China Automat. Congr.*, Chongqing, China, 2023, pp. 8371–8376, doi: 10.1109/CAC59555.2023.10450293.

[24] C. Ding and L. Lu, "A tilting-rotor unmanned aerial vehicle for enhanced aerial locomotion and manipulation capabilities: Design, control, and applications," *IEEE/ASME Trans. Mechatron.*, vol. 26, no. 4, pp. 2237–2248, Aug. 2021, doi: 10.1109/TMECH.2020.3036346.

[25] K. Patnaik, S. Mishra, S. M. R. Sorkhabadi, and W. Zhang, "Design and control of SQUEEZE: A spring-augmented QUadrotor for intEractions with the environment to squeeZE-and-fly," in *Proc. IEEE/RSJ Int. Conf. Intell. Robots Syst.*, Las Vegas, NV, USA, 2020, pp. 1364–1370, doi: 10.1109/IROS45743.2020.9341730.

[26] S. Park et al., "ODAR: Aerial manipulation platform enabling omnidirectional wrench generation," *IEEE/ASME Trans. Mechatron.*, vol. 23, no. 4, pp. 1907–1918, Aug. 2018, doi: 10.1109/TMECH.2018.2848255.

[27] M. Zhao, K. Nagato, K. Okada, M. Inaba, and M. Nakao, "Forceful valve manipulation with arbitrary direction by articulated aerial robot equipped with thrust vectoring apparatus," *IEEE Robot. Automat. Lett.*, vol. 7, no. 2, pp. 4893–4900, Apr. 2022, doi: 10.1109/LRA.2022.3154018.

[28] R. Funada, M. Soliman, T. Ibuki, and M. Sampei, "Hoverable structure transformation for multirotor UAVs with laterally actuated frame links," *Adv. Robot.*, vol. 38, no. 9–10, pp. 684–697, 2024, doi: 10.1080/01691864.2024.2324310.

[29] A. Sakaguchi and K. Yamamoto, "A novel quadrotor with a 3-axis deformable frame using tilting motions of parallel link modules without thrust loss," *IEEE Robot. Automat. Lett.*, vol. 7, no. 4, pp. 9581–9588, Oct. 2022, doi: 10.1109/LRA.2022.3191195.

[30] Y. Wu et al., "Ring-rotor: A novel retractable ring-shaped quadrotor with aerial grasping and transportation capability," *IEEE Robot. Automat. Lett.*, vol. 8, no. 4, pp. 2126–2133, Apr. 2023, doi: 10.1109/LRA.2023.3245499.

[31] M. Xu, Q. De, D. Yu, A. Hu, Z. Liu, and H. Wang, "Biomimetic morphing quadrotor inspired by eagle claw for dynamic grasping," *IEEE Trans. Robot.*, vol. 40, pp. 2513–2528, 2024, doi: 10.1109/TRO.2024.3386616.

[32] T. Anzai, M. Zhao, T. Nishio, F. Shi, K. Okada, and M. Inaba, "Fully autonomous brick pick and place in fields by articulated aerial robot: Results in various outdoor environments," *IEEE Robot. Automat. Mag.*, vol. 31, no. 2, pp. 39–53, Jun. 2024, doi: 10.1109/MRA.2023.3276265.

[33] Y. Qin, W. Xu, A. Lee, and F. Zhang, "Gemini: A compact yet efficient bi-copter UAV for indoor applications," *IEEE Robot. Automat. Lett.*, vol. 5, no. 2, pp. 3213–3220, Apr. 2020, doi: 10.1109/LRA.2020.2974718.

[34] Y. Qin, N. Chen, Y. Cai, W. Xu, and F. Zhang, "Gemini II: Design, modeling, and control of a compact yet efficient servoless bi-copter," *IEEE/ASME Trans. Mechatron.*, vol. 27, no. 6, pp. 4304–4315, Dec. 2022, doi: 10.1109/TMECH.2022.3153587.

[35] Y. Bai and S. Gururajan, "Evaluation of a baseline controller for autonomous 'Figure-8' flights of a morphing geometry quadcopter: Flight performance," *Drones*, vol. 3, no. 3, 2019, Art. no. 70. [Online]. Available: https://www.mdpi.com/2504-446X/3/3/70

[36] A. Desbiez, F. Expert, M. Boyron, J. Diperi, S. Viollet, and F. Ruffier, "X-Morf: A crash-separable quadrotor that morfs its X-geometry in flight," in *Proc. Educ. Develop. Unmanned Aerial Syst. Workshop Res.*, Linköping, Sweden, 2017, pp. 222–227, doi: 10.1109/RED-UAS.2017.8101670.

[37] V. R. Vundela and V. Muralidharan, "Modeling and control of QBQ-Copter: A novel morphing drone," in *Proc. IEEE Region 10 Symp.*, New Delhi, India, 2024, pp. 1–6, doi: 10.1109/TENSYMP61132.2024.10752105.

[38] D. Hu, Z. Pei, J. Shi, and Z. Tang, "Design, modeling and control of a novel morphing quadrotor," *IEEE Robot. Automat. Lett.*, vol. 6, no. 4, pp. 8013–8020, Oct. 2021, doi: 10.1109/LRA.2021.3098302.

[39] G. M. Hoffmann, H. Huang, S. L. Waslander, and C. J. Tomlin, "Quadrotor helicopter flight dynamics and control: Theory and experiment," in *Proc. AIAA Guid., Navig. Control Conf.*, Hilton Head, Aug. 2007, pp. 1–20.

[40] D. Mellinger and V. Kumar, "Minimum snap trajectory generation and control for quadrotors," in *Proc. IEEE Int. Conf. Robot. Automat.*, Shanghai, China, 2011, pp. 2520–2525, doi: 10.1109/ICRA.2011.5980409.

Harsh Modi (Student Member, IEEE) received B.S. degree in mechanical engineering from the Institute of Technology Gandhinagar, Gandhinagar, India, in 2018, and the M.S. degree in mechanical engineering from the Indian Institute of Technology Bombay, Mumbai, India, in 2022. He is currently working toward the Ph.D. degree in mechanical engineering with the J. Mike Walker '66 Department of Mechanical Engineering, Texas A&M University, College Station, TX, USA.

He has also worked in an automobile company Tata Motors Ltd. Pune, India. His research interests include robust control system design and path planning for mobile robotic systems. He is also interested in the concept-to-realization development of novel mechatronics systems.
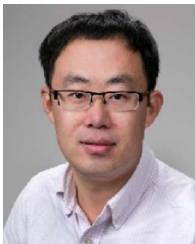
Hao Su (Senior Member, IEEE) received the B.S. degree in automation from the Harbin Institute of Technology, Harbin, China, in 2006, the M.S. degree in mechanical engineering from the State University of New York University, Buffalo, NY, USA, in 2008, and the Ph.D. degree in mechanical engineering from Worcester Polytechnic Institute, Worcester, MA, USA, in 2013.

He was an Associate Professor with the Department of Mechanical and Aerospace Engineering, North Carolina State University, Raleigh, NC, USA, and also in the joint NCSU/UNC Biomedical Engineering Department, University of North Carolina Chapel Hill, Chapel Hill, NC, USA. He was a Research Scientist with Philips Research North America, Cambridge, MA, USA, and, then, a Postdoctoral Fellow with Harvard University, Cambridge, MA, USA, and Wyss Institute for Biologically Inspired Engineering. He is currently an Associate Professor with the Tandon School of Engineering, New York University, New York, NY, USA.

Prof. Su was a recipient of the National Science Foundation CAREER Award and Switzer Distinguished Fellowship of the U.S. Department of Health and Human Services. He is a Technical Editor for ASME/IEEE Transaction on Mechatronics, and an Associate Editor for IEEE Robotics and Automation Magazine, IEEE International Conference on Robotics and Automation, and IEEE/RSJ International Conference on Intelligent Robots and Systems.

Xiao Liang (Member, IEEE) received the B.S. degree from Hunan University, Changsha, China, in 2010, and the M.S. and Ph.D. degrees from the University of California at Berkeley, Berkeley, CA, USA, in 2011 and 2016, respectively, all in civil engineering.

He was an Assistant Professor with the Department of Civil, Structural and Environmental Engineering, University at Buffalo, Buffalo, NY, USA. He is currently an Assistant Professor with the Zachry Department of Civil and Environmental Engineering, Texas A&M University, College Station, TX, USA. His research interests include health monitoring and autonomous inspection of infrastructure systems through advanced data analytics, model-based, and machine learning.
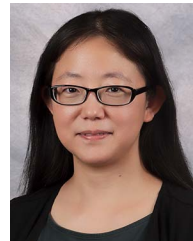
Minghui Zheng (Member, IEEE) received the B.S. degree in engineering mechanics and the M.S. degree in control science and engineering from Beihang University, Beijing, China, in 2008 and 2011, respectively, and the Ph.D. degree in mechanical engineering from the University of California, Berkeley, CA, USA, in 2017.

She was an Associate Professor with the University at Buffalo, Buffalo, NY, USA. She is currently an Associate Professor with the J. Mike Walker '66 Department of Mechanical Engineering, Texas A&M University, College Station, TX, USA. Her research interests include learning, planning, and control with applications to several areas that are of vital importance to manufacturing and robotics.

Dr. Zheng was the recipient of the NSF CAREER Award in 2021.